

PTFO 8-8695: Two Stars, Two Signals, No Planet

L. G. BOUMA,¹ J. N. WINN,¹ G. R. RICKER,² R. VANDERSPEK,² D. W. LATHAM,³ S. SEAGER,^{2,4,5} J. M. JENKINS,⁶ T. BARCLAY,^{7,8}
K. A. COLLINS,³ J. P. DOTY,⁹ D. R. LOUIE,¹⁰ S. N. QUINN,³ M. E. ROSE,⁶ J. C. SMITH,^{6,11} J. VILLASEÑOR,² AND B. WOHLER^{6,11}

¹*Department of Astrophysical Sciences, Princeton University, 4 Ivy Lane, Princeton, NJ 08540, USA*

²*Department of Physics and Kavli Institute for Astrophysics and Space Research, Massachusetts Institute of Technology, Cambridge, MA 02139, USA*

³*Center for Astrophysics | Harvard & Smithsonian, 60 Garden St, Cambridge, MA 02138, USA*

⁴*Department of Earth, Atmospheric and Planetary Sciences, Massachusetts Institute of Technology, Cambridge, MA 02139, USA*

⁵*Department of Aeronautics and Astronautics, MIT, 77 Massachusetts Avenue, Cambridge, MA 02139, USA*

⁶*NASA Ames Research Center, Moffett Field, CA 94035, USA*

⁷*NASA Goddard Space Flight Center, 8800 Greenbelt Road, Greenbelt, MD 20771, USA*

⁸*University of Maryland, Baltimore County, 1000 Hilltop Circle, Baltimore, MD 21250, USA*

⁹*Noqi Aerospace Ltd., 15 Blanchard Avenue, Billerica, MA, 01821, USA*

¹⁰*Department of Astronomy, University of Maryland, College Park, MD 20742, USA*

¹¹*SETI Institute, Mountain View, CA 94043, USA*

(Received May 15, 2020; Revised June 16, 2020; Accepted June 17, 2020)

Submitted to AAS journals.

ABSTRACT

PTFO 8-8695 (CVSO 30) is a star in the 7–10 million year old Orion-OB1a cluster that shows brightness dips that resemble planetary transits. Although strong evidence against the planet hypothesis has been presented, the possibility remains debated in the literature. To obtain further clues, we inspected data from the NASA *Transiting Exoplanet Survey Satellite* (TESS) and the ESA Gaia mission. The Gaia data suggest that PTFO 8-8695 is a binary: the photometric data show it to be overluminous with respect to members of its kinematic group, and the astrometric data are inconsistent with a single star. The TESS light curve shows two different photometric periods. The variability is dominated by a sinusoidal signal with a period of 11.98 hr, presumably caused by stellar rotation. Also present is a 10.76 hr signal consisting of a not-quite sinusoid interrupted by hour-long dips, the type of signal previously interpreted as planetary transits. The phase of the dips is nearly 180° away from the phase of the originally reported dips. As noted previously, this makes them difficult to explain as planetary transits. Instead, we believe that PTFO 8-8695 is a pair of young and rapidly rotating M dwarfs, one of which shows the same “transient-dipper” behavior that has been seen in at least 5 other cases. The origin of these transient dips is still unknown but likely involves circumstellar material.

Keywords: Exoplanet evolution (491), Pre-main sequence stars (1290), Stellar rotation (1629), Variable stars (1761), Low mass stars (2050)

1. INTRODUCTION

We wish PTFO 8-8695b were a planet. It would be quite exceptional. It would be the youngest known transiting¹ hot Jupiter (van Eyken et al. 2012), orbiting a T Tauri star in the Orion-OB1a cluster. It would have the shortest orbital period of any hot Jupiter. With such a short period, it would probably be filling its Roche lobe, and actively losing mass to

its host star. Not only that, but the rapidly-rotating host star is probably oblate enough to cause the planet’s orbit to precess into and out of the transiting configuration on a timescale of years (Barnes et al. 2013; Ciardi et al. 2015; Kamiaka et al. 2015).

Another first would be the direct detection of H α emission from a close-in planet (Johns-Krull et al. 2016b). In addition to the chromospheric H α emission, it seems that there is an additional H α emission with radial velocity variations in phase with the planetary orbit. The average velocity width of the excess H α emission is 87 km s^{−1}, and its equivalent width is 70–80% that of the stellar chromosphere (Johns-Krull et al. 2016b). The proposed explanation is that the emission is

Corresponding author: L. G. Bouma
luke@astro.princeton.edu

¹ Younger hot Jupiters have been reported around V830 Tau, TAP 26, and CI Tau (Johns-Krull et al. 2016a; Donati et al. 2016; Donati et al. 2017; Yu et al. 2017; Biddle et al. 2018; Flagge et al. 2019).

from hot material flowing away from the planet (Johns-Krull et al. 2016b).

However, the observed signals have some peculiarities that make the planet seem even more unusual, to the point that they cast into doubt the premise that PTFO 8-8695b is real. First, the transit-like brightness dips are about three times deeper in optical bandpasses (e.g., *g*-band) than in the near-infrared (e.g., *z*-band) (Onitsuka et al. 2017; Tanimoto et al. 2020). An ordinary atmosphere expected for a Jovian planet would not lead to such a strong color-dependence of the transits. Second, the planet does not seem to emit as much infrared radiation as would be expected for such a hot Jovian planet (Yu et al. 2015). Third, despite measurement attempts by multiple investigators, PTFO 8-8695b does not seem to show the Rossiter effect at the amplitude expected given the rapid stellar rotation and large planet size (Yu et al. 2015; Ciardi et al. 2015). Fourth, the phase of the dips within the overall period of photometric variability has changed drastically over the years since their initial discovery. To counter these objections, it has been proposed that the planet may be much smaller than Jupiter and that the dips are produced by dust clouds emitted from the planet (Tanimoto et al. 2020).

A separate issue is that the brightness dips change shape over many orbital cycles. This was initially explained by Barnes et al. (2013) as the natural effects of gravity darkening. However, Howarth (2016) argued that the necessary amplitude of gravity darkening is too large to be realistic, given the spectroscopically-determined rotation velocity. Additionally, as the gravity-darkened star precessed about its rotation axis, it would show photometric variability that has not been observed.

While the planetary interpretation clearly faces challenges, there is no completely satisfactory alternate explanation. Low-latitude starspots, hot or cold, would struggle to produce photometric features as short as some of the observed dips. High-latitude accretion hotspots might produce the observed $H\alpha$ variability, but require fine-tuning to produce dips of the appropriate duration. Transits by dust clumps or other dusty features are questionable because PTFO 8-8695 does not have a detectable infrared (IR) excess associated with the presence of warm dust (e.g., Yu et al. 2015, Figure 18). In addition, the sublimation times for dust grains of plausible composition could be quite short (Zhan et al. 2019).

A relevant fact is that between 0.1% and 1% of rapidly rotating low-mass stars in $\mathcal{O}(10)$ Myr old associations show short-duration dips as part of their overall periodic variability (Rebull et al. 2018). The dips can persist over months, but their depths often vary, and sometimes change immediately after stellar flares. The explanation proposed by Stauffer et al. (2017) and David et al. (2017) to explain this novel class of variable stars is that a clumpy torus of dust and gas orbits near the Keplerian co-rotation radius. To this point, though, it has not been clear if this explanation applies to PTFO 8-8695, because the determination of the stellar rotation period has been somewhat ambiguous (van Eyken et al. 2012; Koen 2015; Rietz et al. 2016).

We begin in Section 2 by describing newly available observations from TESS (Ricker et al. 2015) and Gaia (Gaia Collaboration et al. 2018). The TESS light curve shows two different periodic signals, which we analyze in Section 3. The Gaia data, analyzed in Section 4, show that PTFO 8-8695 is too bright to be a single star and also suggest it is an astrometric binary. We discuss the pieces of the puzzle in Section 5, and summarize the situation in Section 6. In a postscript, we comment on a recent study by Koen (2020) which reached similar conclusions.

2. THE DATA

2.1. TESS Observations

PTFO 8-8695 (also known as CVSO 30; Briceño et al. 2005) was observed by TESS with Camera 1, CCD 1, from December 15, 2018 until January 6, 2019, during the sixth sector of science operations (Ricker et al. 2015). The star is designated TIC 264461976 in the TESS Input Catalog (Stassun et al. 2018, 2019). The pixel data for an 11×11 array surrounding PTFO 8-8695 were averaged into 2-minute stacks by the onboard computer. Each 2048×2048 image from the CCD was also averaged into 30-minute stacks, and saved as a “full frame image” (FFI).

The 2-minute stacks for PTFO 8-8695 were reduced to light curves by the Science Processing Operations Center (SPOC) at the NASA Ames Research Center (Jenkins et al. 2016). We mainly used the Presearch Data Conditioning Simple Aperture Photometry (PDCSAP) light curve. The PDC light curve is based on pixels chosen to maximize the SNR of the total flux of the target (Bryson et al. 2020). Non-astrophysical variability was removed by fitting out trends common to many stars (Smith et al. 2012; Stumpe et al. 2014).

As an independent check on the 2-minute SPOC light curve, we examined the light curve based upon 30-minute image stacks which was produced as part of the Cluster Difference Imaging Photometric Survey (CDIPS; Bouma et al. 2019). Our CDIPS light curve of choice used a circular aperture with radius 1 pixel.

To clean the data, we removed all points with non-zero quality flags, which indicate known problems (e.g., Tenenbaum & Jenkins 2018). We also masked out the data from the first and last 6 hours of each orbit, since there are often systematic effects in the photometry during those times. Both the CDIPS and PDC light curves showed a discontinuous jump in the last few days of orbit 20, which seemed likely to be an instrumental systematic effect, and led us to mask out the data with timestamps ranging from BJD 2458488.3 until the end of the orbit. The PDC light curve initially had 15,678 points. The quality-flag cut removed 854 points; masking the orbit edges removed an additional 716 points; and removing the data from the final few days of orbit 20 removed an additional 1,079 points. After cleaning, 83% of the initial flux measurements remained.

We normalized the light curve by dividing out the median flux, and then opted to subtract 1.0 to set the median value to zero, which simplified subsequent interpretation. Many of



Figure 1. TESS light curve of PTFO8-8695 (Sector 6, Orbit 19). *Top:* The original (PDCSAP median-subtracted) relative flux. The beat period of 4.48 days is visible by eye. The blue curve is a model including 2 harmonics at the longer period P_ℓ , plus 3 harmonics and a transit at the shorter period P_s . *Upper middle:* Longer-period signal, equal to the original signal minus the shorter-period signal. *Lower middle:* Shorter-period signal, equal to the original signal minus the longer-period signal. *Bottom:* residual relative flux. The data are binned from 2 to 10 minute cadence for convenience in plotting and fitting.

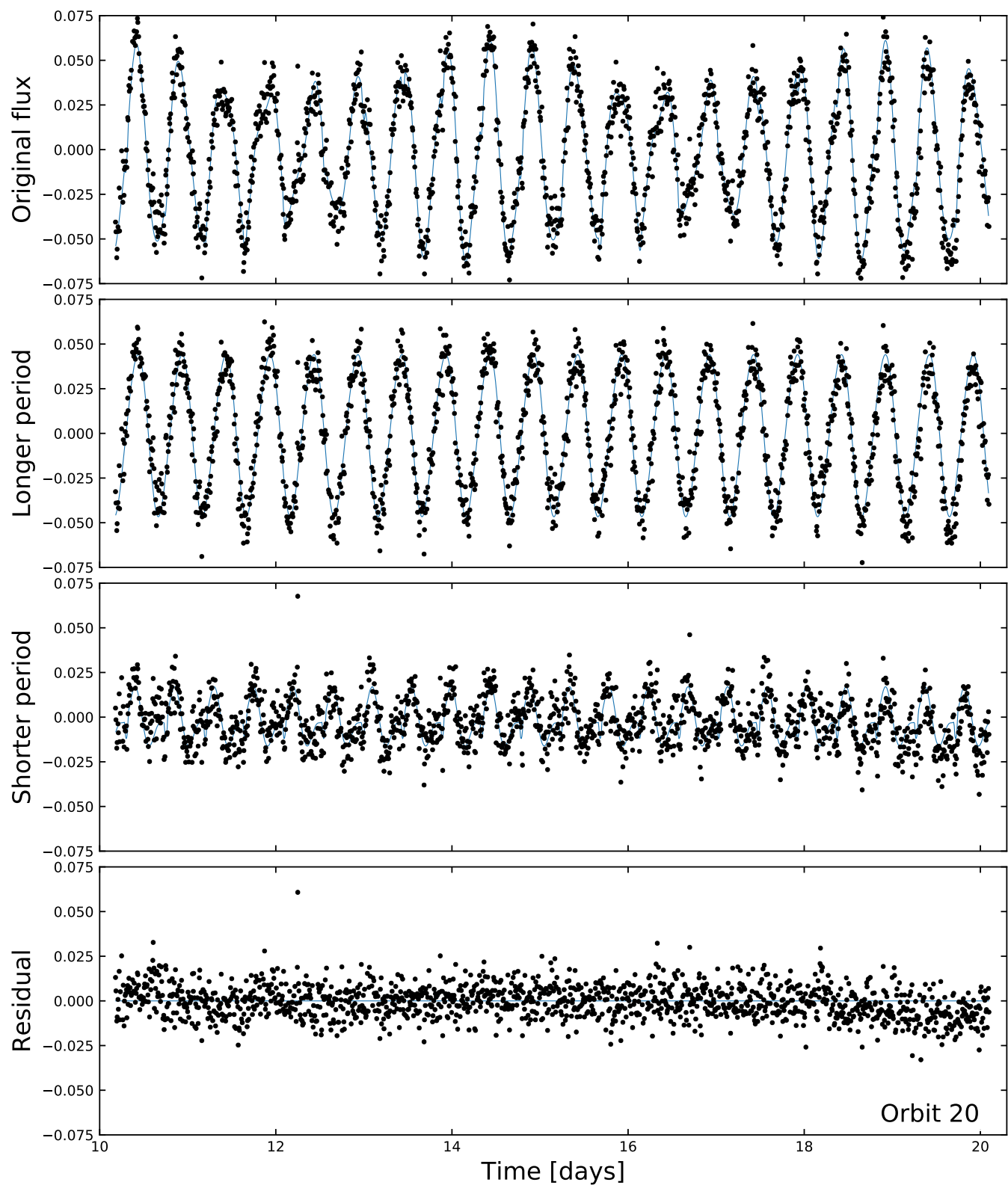


Figure 2. TESS light curve of PTFO8-8695 (Sector 6, Orbit 20). Same format as Figure 1.

these and subsequent processing steps were performed using *astrobase* (Bhatti et al. 2018).

2.2. Gaia Observations

2.2.1. Astrometric measurements

Between July 25, 2014 and May 23, 2016, Gaia measured about 300 billion centroid positions of 1.6 billion stars (Gaia Collaboration et al. 2016; Lindegren et al. 2018; Gaia Collaboration et al. 2018). For the Gaia second data release (DR2), these CCD observations were used to determine positions, proper motions, and parallaxes of the brightest 1.3 billion stars (Lindegren et al. 2018). For PTFO8-8695, there were 121 “good” observations, *i.e.*, observations that were not strongly down-weighted in the astrometric solution. PTFO8-8695 was assigned the Gaia DR2 identifier 3222255959210123904. Its brightness was measured using selected bands (*G*, *R_p*, and *B_p*) of the Gaia Radial Velocity Spectrometer (Cropper et al. 2018; Evans et al. 2018). We accessed the pipeline parameters for PTFO8-8695 using the Gaia archive².

The majority of Gaia’s derived parameters for PTFO8-8695 agree with expectations based on previous studies (Briceño et al. 2005; van Eyken et al. 2012). The main novelty is that Gaia DR2 reported a 10.3σ “astrometric excess”, indicating that the residuals to the best-fitting astrometric model were larger than expected based on the statistical uncertainties. We comment on the significance and interpretation of this excess in Section 4.

2.2.2. Hierarchical Cluster Membership

Gaia also provided astrometric parameters for tens of thousands of young stars in the Orion complex. Stellar populations in giant molecular cloud complexes are not monolithic; substructured groups are the norm (Briceño et al. 2007). The Orion molecular cloud complex in particular has numerous subgroups, with ages ranging from 0.5 to 15 Myr. See, for instance, Briceño et al. (2005); Jeffries et al. (2006); Briceño et al. (2007); Kounkel et al. (2018) and Briceño et al. (2019).

PTFO8-8695 was initially designated CVSO 30 and identified as a member of the Orion OB1a sub-association by Briceño et al. (2005), based on photometry and spectroscopy. Later work by Briceño et al. (2007) clarified that PTFO8-8695 is in a kinematically distinct subgroup of Orion OB1a, named the “25Ori” group after its brightest member. They reported that the 25Ori group has an isochrone age of 7–10 Myr, and a smaller fraction of stars with disks than younger nearby sub-associations (Hernández et al. 2007).

With the Gaia astrometry, it has become clear that 25Ori itself has distinct subgroups (Kounkel et al. 2018; Briceño et al. 2019). In describing the cluster membership of PTFO8-8695, we follow the notation and results of Kounkel et al. (2018). These authors combined astrometric data from Gaia DR2 with near-infrared spectra from APOGEE-2 (Gunn et al.

2006; Majewski et al. 2017; Blanton et al. 2017; Zasowski et al. 2017; Cottle et al. 2018). They performed a hierarchical clustering on the six-dimensional position and velocity information to identify subgroups within the Orion complex. From smallest to largest, PTFO8-8695 was identified as a member of the following hierarchical subgroups:

$$25\text{Ori-1} \subset 25\text{Ori} \subset \text{Orion OB1a} \subset \text{Orion D}, \quad (1)$$

where ‘ \subset ’ means ‘is a proper subset of’. 25Ori-1 is the largest subgroup of 25Ori, with 149 identified members. The mean age of the 25Ori-1 subgroup, determined by fitting isochrones to group members with APOGEE effective temperatures and Gaia parallaxes, was determined to be 8.5 ± 1.2 Myr (see Kounkel et al. 2018, Section 2.3). Kounkel et al. (2018) also identified seven smaller groups in the Orion complex near the Be star 25Ori. These groups received sequential identifiers, *e.g.*, 25Ori-2 (Age = 12.9 ± 2.8 Myr; see also Briceño et al. 2019).

While all members of the Orion complex are young relative to the field, these considerations are essential for assessing photometric evidence for the binarity of PTFO8-8695, because of the degeneracy between stellar luminosity and age for pre-main-sequence stars. Having a clean sample of reference stars that are tightly associated with PTFO8-8695 — both spatially and kinematically — minimizes contamination not only from field stars, but also from older and younger members of the Orion complex.

3. TESS ANALYSIS

3.1. Inspection

Our initial inspection of the TESS light curve, in both its 2-minute PDCSAP and 30-minute FFI forms, showed a strong sinusoidal beat signal (Figures 1 and 2, top panel). As a precursor to more detailed analysis, we calculated generalized Lomb-Scargle periodograms using *astrobase* (Lomb 1976; Scargle 1982; VanderPlas & Ivezić 2015; Bhatti et al. 2018). The tallest peak occurs at 11.98 hr and a second strong peak occurs at 10.76 hr. We will refer to these two periods as the “longer period” P_ℓ and the “shorter period” P_s . Lower-power harmonics of both signals are also present.

The peak-to-peak maximum amplitude of the light curve, when the two signals interfere constructively, is about 14%. During the times of destructive interference, the peak-to-peak amplitude is about 6%. Assuming the signals are mainly sinusoidal, simple algebra tells us that the peak-to-peak amplitudes should be about 10% for the longer-period signal, and 4% for the shorter-period signal. To view the phase-folded light curves of the longer-period signal, we subtracted the best-fitting sinusoid with a period equal to P_s . The resulting light curve appears smooth and nearly sinusoidal. But after subtracting the best-fitting sinusoid with a period equal to P_ℓ , visual inspection of the phase-folded light curve revealed substructure resembling the “dips” seen in previous observations. In particular, there was a $\approx 1\%$ dip lasting about an hour. These initial impressions turned out to be consistent with the results of our more complicated analysis, described below.

² gea.esac.esa.int/archive/

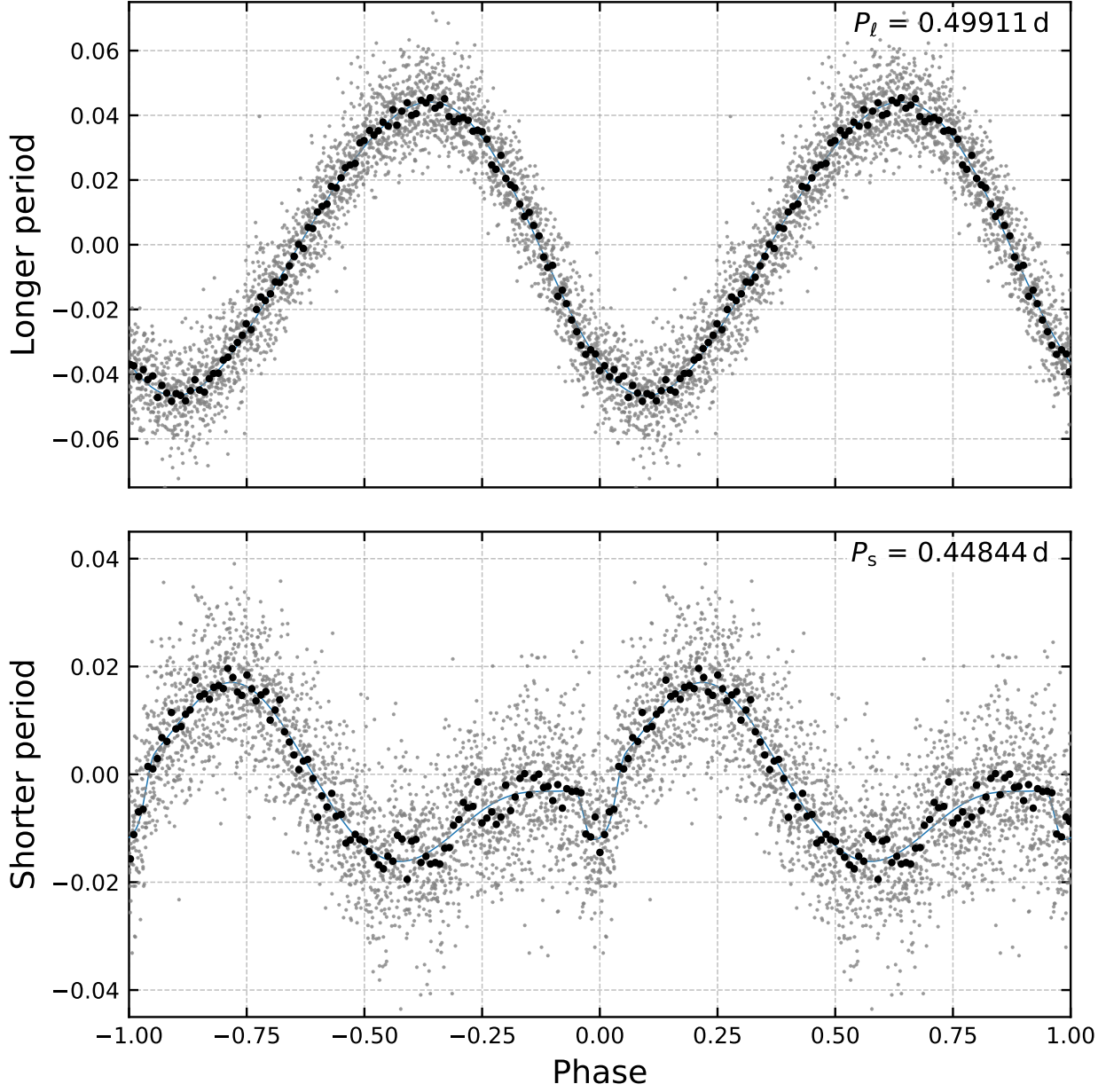


Figure 3. Phase-folded longer and shorter-period signals. *Top:* The longer-period signal. *Bottom:* The shorter-period signal. The phase is defined such that the dip occurs at zero phase. Gray points are the PDCSAP data binned to 10-minute cadence. Black points are binned to 100 points per period. The model (blue line) includes 2 harmonics at the longer period, plus 3 harmonics and a transit at the shorter period.

3.2. Light Curve Model

We fitted a model to the light curve consisting of a linear combination of Fourier modes with periods P_s and P_ℓ , as well as a number of harmonics chosen as described below. To try accounting for the dips, we also added an analytic transit model with period P_s . Symbolically, the total flux f is given as

$$f = f_s + f_\ell = f_{\text{transit},s} + f_{\text{Fourier},s} + f_{\text{Fourier},\ell}, \quad (2)$$

where f_s is the flux at the shorter period, and f_ℓ is the flux at the longer period. Writing out the Fourier terms explicitly,

$$f = f_{\text{transit},s} + \sum_{n=1}^{N_s} A_n \sin(n\omega_s t) + \sum_{n=1}^{N_s} B_n \cos(n\omega_s t) + \sum_{m=1}^{N_\ell} A_m \sin(m[\omega_\ell t + \phi_\ell]) + \sum_{m=1}^{N_\ell} B_m \cos(m[\omega_\ell t + \phi_\ell]), \quad (3)$$

where N_s and N_ℓ are the total number of modes at the shorter and longer periods, respectively, A_i and B_i are the amplitudes of each mode (which can be positive or negative), and ω_ℓ

and ω_s are the angular frequencies of the longer-period and shorter-period signals. By not including a phase parameter in the shorter-period model, we have implicitly defined the zero point of the phase scale. The relative phase of the longer-period model is specified by the phase parameter ϕ_ℓ . Since we did not know in advance how many harmonics would be appropriate to include in the model, we considered a number of different choices for N_s and N_ℓ , and used the Bayesian information criterion to select the final model (Table 1).

The free parameters are as follows. The transit model parameters are the impact parameter, the planet-to-star radius ratio, two quadratic limb darkening parameters, the planet’s orbital period (set equal to P_s) the time of a particular transit, and the mean flux. We sampled the stellar radius and mass from prior probability distributions, implicitly defining the stellar density which (together with the orbital period) sets the transit timescale. There are also the parameters defining the Fourier modes. As an example, one possible model consists of a transit, $N_s = 2$ sines and cosines at the shorter period, plus $N_\ell = 1$ sine and cosine at the longer period. There are $2N_s = 4$ additional Fourier amplitudes at the shorter period, plus $2N_\ell = 2$ Fourier amplitudes at the longer period, as well as P_ℓ itself and the relative phase ϕ_ℓ . The total number of parameters is 17 for this case.

We implemented and fitted the models using `PyMC3`, which is built on `theano` (Salvatier et al. 2016; Theano Development Team 2016). For the Fourier terms, we used the default math operators. For the exoplanet transit, we used the model and derivatives implemented in the `exoplanet` code (Foreman-Mackey et al. 2020). Our priors are listed in Table 2. To speed up the fitting process, we averaged the 2-minute light curve into 10-minute samples. We correspondingly scaled down the uncertainties in the flux measurements by a factor of $\sqrt{5}$. Before sampling, we initialized each model with the parameters of the maximum *a posteriori* (MAP) model. We then assumed a Gaussian likelihood, and sampled using `PyMC3`’s gradient-based No-U-Turn Sampler (Hoffman & Gelman 2014), and used \hat{R} as our convergence diagnostic (Gelman & Rubin 1992). We tested our ability to successfully recover injected parameters using synthetic data before fitting the PTFO 8-8695 light curves.

3.3. Fitting Results

We considered nine models, with the number of modes per frequency (N_s and N_ℓ) ranging from one to three. To select our preferred model, we used the Bayesian information criterion (Table 1). The model with the lowest BIC had three modes at the shorter 10.76 hr period, and two modes at the longer 11.98 hr period. The other models had BIC values that implied significantly less support (Burnham & Anderson 2016). All nine models have reduced χ^2 values ranging between 1.21 and 1.68, which suggests a plausible though imperfect agreement between the data and the model to within the formal uncertainties. Table 2 gives the best-fitting parameters for the preferred model, which has the lowest BIC value.

To explore where each model succeeded and failed, we split the original signal into its respective components (Figures 1 and 2). We also examined the phase-folded signals (Figure 3).

In every model, the 11.98 hr variability is a simple sinusoid with peak-to-peak amplitude $\approx 10\%$. The 10.76 hr variability is always more complex. The overall impression is of a distorted sinusoidal function, with a peak-to-peak amplitude of about 4%. The asymmetric sinusoid rises to a maximum near phase 0.25, and reaches minimum brightness between phases -0.5 and -0.25 . Between phases -0.5 and 0.0 there appears to be complex shorter-timescale variability, ending with a “dip” of depth $\approx 1.2\%$, lasting ≈ 0.75 hours. The fact that our preferred model has three rather than two “short period” harmonics is linked to the degree of curvature required between phases -0.5 and -0.05 : the analogous $(N_\ell, N_s) = (2, 2)$ model prefers a longer transit duration, but does not fit the out-of-transit curvature as well, particularly immediately before ingress.

The periodogram of the residuals between the data and the preferred model shows a barely significant and poorly-resolved peak at ≈ 8 days, consistent with the visual impression of some slower trends in the bottom rows of Figures 1 and 2.

4. TESTS FOR BINARITY

4.1. Visual Binarity

The portion of the sky subtended by each TESS pixel is about $21''$ on a side. Before making any interpretations, we needed to consider whether light from neighboring stars could have contributed to the photometric signal we are attributing to PTFO 8-8695. The scene is shown in Figure 4. In the upper panels, the pixels used to measure the background level in the SPOC light curve are indicated with ‘x’ hatching, and the pixels used in the final light curve aperture are shown with ‘/’ hatching.

The target star, PTFO 8-8695 (TIC 264461976), has a T -band magnitude of 14.0, and its position is shown with a star. The other (unlabeled) star inside the target aperture, TIC 264461979, has $T = 16.8$ and so cannot contribute more than about 10% to the total signal. The only other known star that is sufficiently close and bright that its light might contaminate the signal from the target star is TIC 264461980, with $T = 14.8$. This star, we dub “Star A”, is $23.6''$ northwest of the target. Based on the magnitude difference, Star A could contribute flux variations as large as 48% of the flux of the target star.

The variability of PTFO 8-8695 with a period consistent with P_s had already been observed based on images with arc-second resolution. Thus, our main concern regarding blending was whether the longer-period signal with period P_ℓ originated from PTFO 8-8695, or from Star A. We took two approaches to investigate the source of the long-period signal.

First, we examined the CDIPS FFI light curves of the target, which are available on MAST (Bouma et al. 2019). Three light curves are available, based on photometric apertures with a radius of 1, 1.5, or 2.5 pixels. The maximal

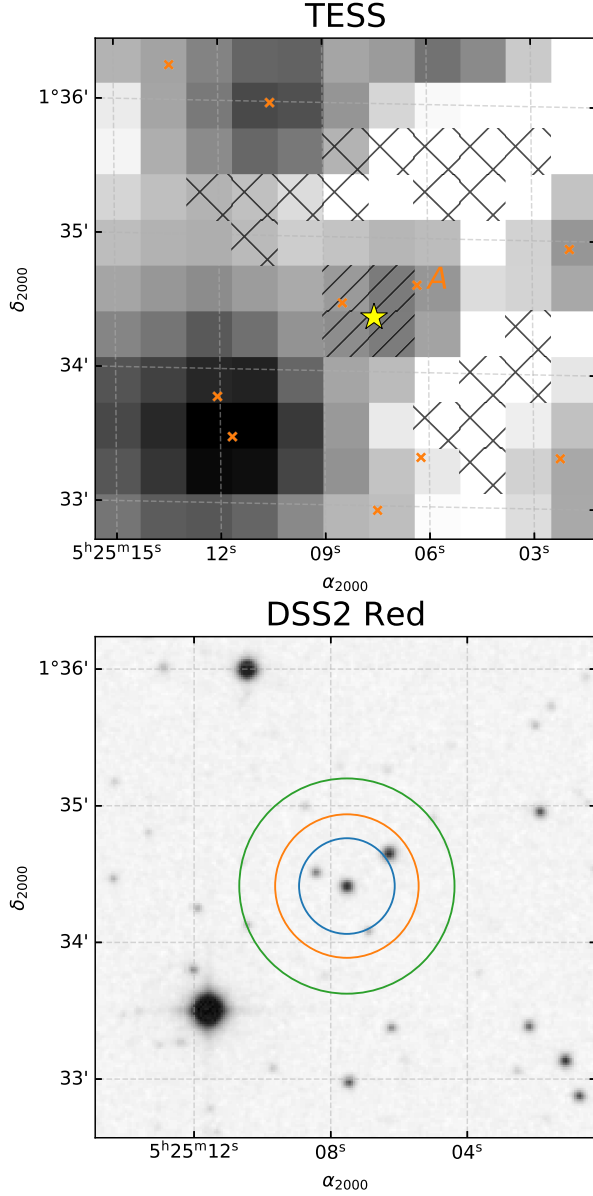


Figure 4. Scene used for blend analysis. *Top:* Mean TESS image of PTFO8-8695 over Sector 6, with a logarithmic grayscale. The yellow star is the position of PTFO8-8695. Orange crosses are neighboring stars with $T < 17$. The X and / hatches show the apertures used to measure the background and target star flux, respectively. *Bottom:* Digitized Sky Survey R -band image of the same field, with a linear grayscale. The circles show the apertures of radii 1, 1.5, and 2.25 pixels used in our blend analysis. To the northwest of PTFO8-8695 and between the blue and orange circles is “Star A”, the only star bright and close enough to be contributing to the signal attributed to PTFO8-8695. However, the pixel-level TESS data showed that Star A is not the source of the observed variability (see Section 4.1).

peak-to-peak beat amplitude was the same to within a percent, regardless of the size of the photometric aperture that

was used to create the light curve. If Star A were the source of the long-period variability, we would expect the peak variability amplitude to be smallest in the 1 pixel aperture, based on the separation of the sources (Figure 4, bottom). From this test alone, it seems unlikely that Star A is the source of the long-period signal.

Second, we examined the 2-minute light curve of each individual pixel in the scene, using the interactive tools implemented in `lightkurve` (Lightcurve Collaboration et al. 2018). If Star A were the source of the long-period variability, we would expect the pixels nearest to Star A to show a sinusoidal signal with amplitude exceeding 10%. The data do not show this pattern. The data from the pixel directly below Star A does not show any sinusoidal variability; the peak-to-peak variability seen in that pixel is $\lesssim 8\%$. In contrast, the southeastern-most pixel within the PTFO8-8695 aperture (the pixel furthest from Star A that was used in the optimal aperture) shows the longer-period sinusoidal variability signal with an amplitude of 14%. We conclude that within the resolution of the Gaia DR2 source catalog, the P_s and P_ℓ signals originate from PTFO8-8695. Based on the work of Ziegler et al. (2018), we can surmise that stellar companions with separations wider than $\approx 1''$ (349 AU) and within $\Delta G \approx 3$ magnitudes of PTFO8-8695 would have likely been detected through this approach.

Stronger constraints on possible stellar companions were obtained by van Eyken et al. (2012) through high-resolution imaging with the NIRC2 camera on the Keck II 10m telescope. They reported $3\text{-}\sigma$ H -band magnitude difference limits of 4.3, 6.4, and 8.9 at angular separations of 0.25, 0.5, and 1.0 arcseconds (87, 175, and 349 AU). They also detected a point source 7.0 magnitudes fainter than the target, and $1.8''$ to the north-east (which is not included in the Gaia DR2 catalog). Due to its relative faintness, this object cannot be the source of the shorter and longer-period TESS signals.³

4.2. Photometric Binarity

We also used the Gaia data to see if the observed luminosity of PTFO8-8695 is too high to be from a single star, i.e., if the object is a “photometric binary.” To assemble a set of stars coeval with PTFO8-8695, we used the 25Ori-1 members identified by Kounkel et al. (2018), and discussed in Section 2.2.2. To define a set of non-member stars that nonetheless are subject to similar selection criteria, we defined the reference “neighborhood” as the group of at most 10^4 randomly selected non-member stars within 5 standard deviations of the mean values of the right ascension, declination, and parallax of 25Ori-1. We queried Gaia DR2 for these stars using `astroquery` (Ginsburg et al. 2018). This yielded 1,819 neighbors. While some of these stars may indeed be members of the Orion complex, or even of 25Ori-1, enforcing this cut on positions and parallaxes ensures that we

³ This point source was claimed to be a potential planetary-mass object (Schmidt et al. 2016). Subsequent analysis of its colors showed that it is a background star (Lee & Chiang 2018).

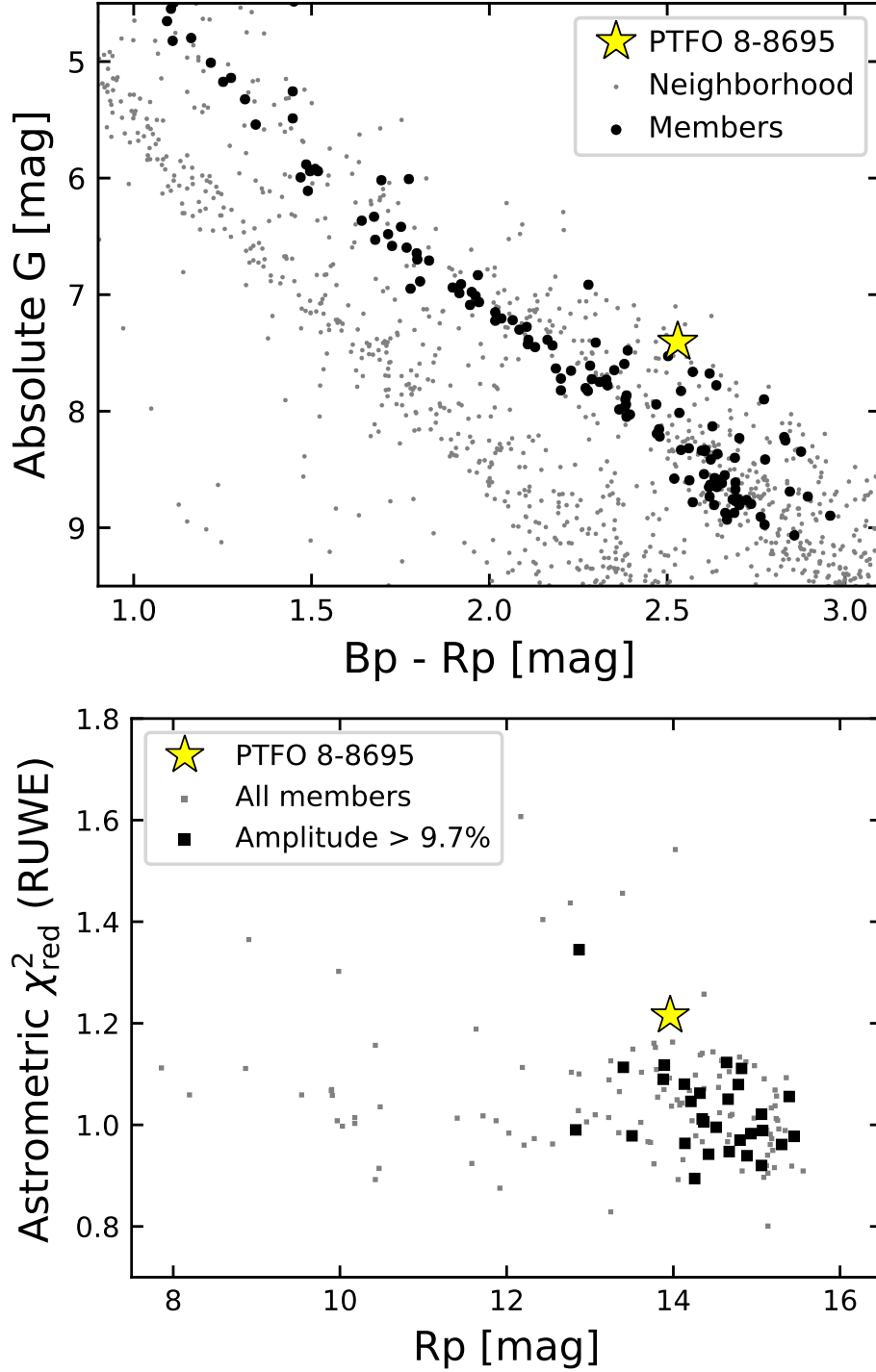


Figure 5. Evidence for binarity in PTFO 8-8695. *Top:* Hertzsprung-Russell diagram of PTFO 8-8695 and late-type members of 25 Ori-1. Black circles are members of the 25 Ori-1 group identified by Kounkel et al. (2018). Gray circles are stars in the “neighborhood”, i.e., non-member stars for which the right ascension, declination, and parallax are within 5 standard deviations of the mean values for 25 Ori-1. The neighborhood contains members of the Orion complex with its full spread of ages, in addition to field interlopers. G denotes the Gaia broadband magnitude, Bp Gaia blue, Rp Gaia red, and ω_{as} the parallax in arcseconds. The x -axis limits are chosen to display only the K and M dwarfs, accentuating PTFO 8-8695’s separation from the single-star sequence. *Bottom:* Renormalized astrometric unit weight error (RUWE) versus Rp magnitude for 25 Ori-1 members. The single-source astrometric model for PTFO 8-8695 provides a poor fit to the data, which could be due to either stellar variability or binarity. But since cluster members that are at least as variable as PTFO 8-8695 show lower astrometric excesses (black squares), binarity is the likely reason.

are comparing stars with similar amounts of interstellar reddening.

We examined the resulting five-dimensional distribution of right ascension, declination, proper motion in both directions, and parallax. The first point we noted was that 25 Ori-1 is a clearly defined over-density in each dimension: the cluster was confirmed to exist, and to be distinct from the neighborhood. The second point we noted is that PTFO 8-8695 belongs to the cluster, based on its properties in each of these dimensions.

Figure 5 shows the HR diagram we constructed from the data. The diagram shows that PTFO 8-8695 is ≈ 0.75 magnitudes brighter than the average 25 Ori-1 star of the same color. In other words, it is about twice as bright as expected for a single star in the cluster. It also seems to be part of a “photometric binary” track that runs above and parallel to the main track.

The implication is that either (i) PTFO 8-8695 is notably younger than the kinematically identical 25 Ori-1 members, or (ii) PTFO 8-8695 is a binary with two components of nearly equal brightness. Since there is no other reason to suspect an age difference, and because the source showed two separate photometric signals with similar but distinct periods, the binary interpretation seems more probable.

4.3. Astrometric Binarity

A separate line of evidence for binarity is the Gaia DR2 astrometry. As noted in Section 2, the Gaia DR2 astrometric solution for PTFO 8-8695 shows a 10.3σ “astrometric excess”, a parameter that quantifies the degree to which a single-star model fails to fit the astrometric measurements. Specifically, the single-source astrometric model yielded $\chi^2 = 325.2$. There are 121 astrometric measurements, and 5 free parameters, and therefore 116 degrees of freedom. The reduced χ^2 is 2.80. While the majority of stars with comparable brightness in Gaia do not show such poor goodness-of-fit, many M dwarfs do, because of a color-dependent term in the mission’s PSF model (see Lindegren et al. 2018, Appendix A). The reduced χ^2 has been “renormalized” to account for this, yielding a modified statistic called the renormalized unit weight error (RUWE⁴).

We acquired the RUWE for each of the 149 members in 25 Ori-1 identified by identified by Kounkel et al. (2018). We then queried the CDIPS light curve database at MAST (Bouma et al. 2019) to find the subset of members that were at least as variable as PTFO 8-8695. We measured the variability amplitude by taking the difference between the 95th and 5th percentiles of the flux measurements. This yielded 30 stars of equal or greater variability. The lower panel of Figure 5 shows the RUWE of these stars as a function of stellar brightness. PTFO 8-8695 is at the 93rd percentile of equally-variable stars within the 25 Ori-1 group. Two of the thirty stars with variability amplitudes greater than 9.7%

showed higher RUWE. One was CVSO 35, which has a TESS light curve that varies by 2 magnitudes, and shows both a strong Wide-field Infrared Survey Explorer (WISE, Wright et al. 2010) IR excess and also a $10\mu\text{m}$ silicate emission feature (Maucó et al. 2018). The other star was GAIA DR2 3222210363837122048.

Potential explanations for an elevated RUWE include photometric variability and unresolved stellar binarity (e.g., Rizzuto et al. 2018; Belokurov et al. 2020). If photometric variability were the root cause, we would expect stars with similar brightness and color in the same kinematic group of Orion to show similar astrometric excesses, because the majority of young stars are highly variable. However relative to other M-dwarf group members with comparable brightnesses and variability characteristics, PTFO 8-8695 still stands out by virtue of its failure to conform to a single-star astrometric model. This supports the interpretation that PTFO 8-8695 is a binary star.

We will have to wait for the next data release of the Gaia mission for a more definitive determination of whether the astrometric excess is caused by stellar binarity or photometric variability. Nonetheless the fact that comparably variable stars do not show comparably large astrometric excesses suggests that stellar binarity is indeed the root cause.

4.4. Radial Velocity Binarity

Radial velocity (RV) measurements over sufficiently long timescales could also reveal the presence of multiple stars in this system. Unfortunately, the available RV data for PTFO 8-8695 is sparse, presumably due to the difficulties of performing RV observations of such a faint and rapidly rotating star. The RV datasets with the longest time baselines we could find in the literature were those reported by van Eyken et al. (2012). These included 5 Keck/HIRES measurements acquired over 10 days in April 2011, and 4 HET/HRS measurements acquired over 10 days in February 2011. The root-mean-squared RV over each 10-day span was $\approx 2\text{ km s}^{-1}$, consistent with the measurement precision. Although van Eyken et al. (2012) tried a CCF-based RV reduction technique, they eventually found that manually selecting absorption lines and measuring line centroids was more effective. While Yu et al. (2015) acquired 22 further Keck/HIRES spectra over one night in December 2013, those points were not reduced to velocities. Further radial-velocity observations could potentially confirm or refute the presence of binary companions.

5. DISCUSSION

5.1. Longer-Period Signal

The standard interpretation for 11.98 hr nearly sinusoidal modulations of a pre-main-sequence M dwarf is stellar rotation. This is the dominant signal in the system with 10% amplitude, and there is no evidence to suggest that this signal has any other origin.

In their report on the discovery of the unusual photometric variability, van Eyken et al. (2012) saw an alias of the longer-period signal (e.g., their Figure 7), in the form of a peak in the periodogram at $23.96 \pm 0.15\text{ hr}$. They ascribed it to their

⁴ See the Gaia DPAC technical note GAIA-C3-TN-LU-LL-124-01, http://www.rssd.esa.int/doc_fetch.php?id=3757412, accessed 2020-04-27.

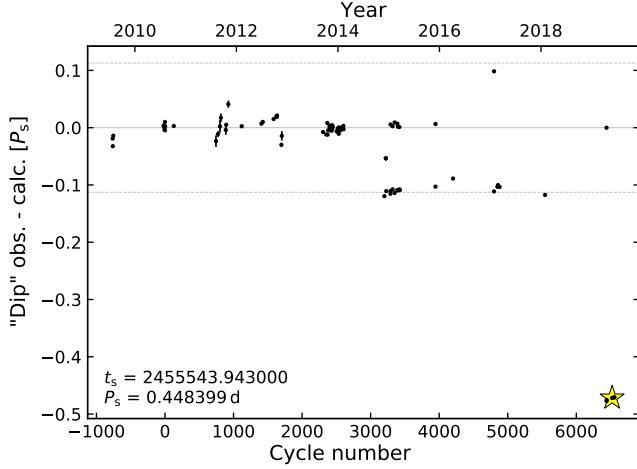


Figure 6. Timing residuals for PTFO 8-8695b based on a decade of monitoring. Black points are times of dips, minus the indicated linear ephemeris. The phase of the shorter-period signal is plotted on the y-axis. The star symbol represents the TESS ephemeris. Dips were observed by [van Eyken et al. \(2012\)](#), [Ciardi et al. \(2015\)](#), [Yu et al. \(2015\)](#), [Raetz et al. \(2016\)](#), [Onitsuka et al. \(2017\)](#), and [Tanimoto et al. \(2020\)](#). Certain dips (e.g., the one at phase 0 in mid-2019) are consistent with noise, and were likely reported because dips were expected, rather than convincingly observed. Horizontal dashed lines are drawn at $\pm(P_\ell - P_s)/P_s$, highlighting a possible numerical coincidence. The orbital phase observed by TESS (lower-right) is consistent with that of [Tanimoto et al. \(2020\)](#).

observing cadence, because of its close correspondence to the sidereal day. Our pixel-level analysis showed that the signal is specific to only pixels near PTFO 8-8695, and no other pixels. We therefore conclude that the signal is not an artifact of systematic errors.

We are not the first to reach the conclusion that the long period sinusoidal modulation is astrophysical. [Koen \(2015\)](#) identified the same modes and aliases as [van Eyken et al. \(2012\)](#), and argued that the signal was astrophysical, even if the exact period was still unclear. Using photometry from the YETI global telescope network, [Raetz et al. \(2016\)](#) came to the conclusion that the 11.98 hr signal was indeed from stellar rotation. The TESS data strongly support this conclusion.

5.2. Shorter-Period Signal, Including the “Dip”

The TESS light curve shows a dip that lasts about 45 minutes, and recurs every 10.76 hours (Figures 1, 2, 3). The dip duration is roughly the same as that observed by previous investigators ([van Eyken et al. 2012](#); [Yu et al. 2015](#)). The 1.2% depth is similar to what has been observed in the near-infrared ([Onitsuka et al. 2017](#)). However the dip depth seems likely to have evolved over time between being not present at all, to a maximum of $\approx 5\%$ (e.g., [Koen 2015](#); [Yu et al. 2015](#); [Tanimoto et al. 2020](#)).

An interesting feature of the sequence of dips is that the phase of the dips has been observed to change with time ([Yu et al. 2015](#)). In fact, [Tanimoto et al. \(2020\)](#) provided stark

evidence for different behavior altogether: over a timespan of years, the dip “split” into distinct groups at particular phases. See, for instance, their Figures 2 through 4. Fitting a decade of observations, they provided the following constant-period ephemeris, which we did not find any need to update:

$$\begin{aligned} t_0 \text{ BJD}_{\text{TDB}} &= 2455543.943 \pm 0.002 \\ P &= 0.4483993 \pm 0.0000006 \text{ d.} \end{aligned} \quad (4)$$

Figure 6 shows the differences between the observed “mid-transit” times of the dips and the times calculated using Equation 4. The phase of the dips seen by TESS (yellow star) agrees with the independent December 2018 measurements by [Tanimoto et al. \(2020\)](#): either the dip abruptly shifted phase over the past decade or, more likely, there are multiple dips that have come and gone at different phases.

Figure 6 shows two additional strange features: (i) multiple dips per cycle, and (ii) a set of dips at a phase that is numerically coincident with $(P_\ell - P_s)/P_s$. The observation of multiple dips per cycle in 2015 was seen independently by both [Yu et al. \(2015\)](#) and [Tanimoto et al. \(2020\)](#). It therefore seems credible. Inspecting the [Tanimoto et al. \(2020\)](#) light curves, the claim of multiple dips per cycle in December 2018 at phase 0 and -0.47 seems less plausible. The dips at phase -0.47 are strongly detected, while the suggested dip at phase 0 is not clearly detected.

We are not sure what to make of the numerical coincidence. The ratio of long to short periods is roughly 10:9. It is not clear that this would obviously translate into an observational bias unless, by some fluke, three season’s worth of observations managed to only observe every ninth dip. This is of course not the case, and we therefore leave this curiosity as observation *sans* interpretation.

5.3. Short Period Modulation Outside of Dips

Visually, the out-of-dip modulation at the 10.76 hr period resembles a slightly asymmetric sinusoid (Figure 3). The best model has non-zero amplitudes for both the first and second harmonics (Table 2). The third harmonic is formally present with marginal ($\approx 2\sigma$) significance. The first sine and cosine harmonic both have amplitudes of roughly $0.90 \pm 0.04\%$. The second sine harmonic has amplitude $0.16 \pm 0.04\%$, so is non-zero at a significance of $\approx 4\sigma$. The second cosine harmonic has an amplitude of $-0.55 \pm 0.03\%$. In our sign convention, the fact that it is negative means that this component peaks at phase 0.25 and 0.75, i.e., the quadratures of the orbit.

5.3.1. Ellipsoidal Variability?

If there were a giant planet transiting PTFO 8-8695, it would tidally distort the host star, and cause ellipsoidal photometric modulations that peak at the quadratures (see [Shporer 2017](#)). Interpreting the second cosine harmonic as planet-induced tidal distortion, it would imply a minimum planet mass $M_p \sin i$ of $3.8 M_{\text{Jup}}$. For this estimate, we assumed $R_* = 1.39 R_\odot$, and $M_* = 0.39 M_\odot$ ([van Eyken et al. 2012](#)). This ellipsoidal amplitude is larger than the typical

modulations induced by close-in giant planets because the host star is puffy, and still on the pre-main-sequence.

The planetary interpretation however does not readily explain the large first sine and cosine harmonics. Interpreting the sine component as Doppler beaming would imply a secondary mass greater than the primary ($0.86 M_{\odot}$). Interpreting the cosine component as reflected or emitted light from the planet’s surface is nonsensical because the sign is wrong—the planet would need to be *absorbing* light.

5.3.2. Similar Light Curves

When physical explanations are not forthcoming, we often resort to taxonomy. By searching the literature, we found about a dozen light curves with similar morphologies to PTFO8-8695, drawn from surveys of low-mass weak-lined T Tauri stars in regions including ρ Oph, Upper Sco, Taurus, and perhaps the Pleiades (Parks et al. 2014; Rebull et al. 2016; David et al. 2017; Stauffer et al. 2017, 2018; Rebull et al. 2018, 2020). The clearest matches came from K2 (Howell et al. 2014), but a few analogs were potentially also found using 2MASS (YMW 1C and YMW 10C; Parks et al. 2014) and CoRoT (Stauffer et al. 2015). We downloaded a subset of the K2 light curves from MAST, opting for the EVEREST reductions (Luger et al. 2016, 2018). They are plotted in Figure 7.

These light curves have been phenomenologically classified as “persistent flux dips” or “transient flux dips”, based on whether their depths and durations show variability over the 90-day K2 campaigns (Stauffer et al. 2017). In the terminology of Stauffer et al. (2017), these objects are morphologically distinct from “scallop shell” light curves, and are present in stars at more advanced evolutionary disk stages than the “dipper” stars (Ansdell et al. 2016; Bodman et al. 2017; Cody & Hillenbrand 2018). The persistent and transient flux dip stars all show angular dips that are cannot be explained as the effects of starspots. These stars typically have the following things in common:

1. They are weak-lined T Tauri stars (under the definition of *e.g.*, Fang et al. 2009).
2. The spectral type is M2 to M5 (*e.g.*, Rebull et al. 2018, Figure 20).
3. The age is typically $\lesssim 100$ Myr.⁵
4. The light curves show shallow, angular dips, superposed on large-amplitude smooth variability at or near 1:1 synchronicity. The smooth variability is interpreted as stellar rotation.
5. The rotation is rapid, with a period that is usually between 0.5 and 2.0 days.

⁵ At present, the oldest observed “scallop” are in the Pleiades (Rebull et al. 2016). One of these, EPIC 211013604, might meet the “persistent dip” classification. If so, it is the oldest known.

6. There is rarely any infrared excess that is detectable in the WISE data (never any W4 detection; only a few W3 detections).
7. They sometimes show multiple dips per cycle.
8. The dip depths, durations, and phases can vary over just a few cycles (*e.g.*, EPIC 204143627).
9. The dip depths can change after flares.
10. They are rare at a population level, with an occurrence rate between 0.1–1% of young M2–M5 stars (Rebull et al. 2018).

The 10.76 hr signal in PTFO8-8695 meets all of these criteria. While this was mentioned by Stauffer et al. (2017), the asymmetric out-of-dip modulation shown by the TESS data solidifies the connection.

There are two crucial additional points concerning the transient flux dips. First, the dip durations seem to scale linearly with the photometric periods (Stauffer et al. 2017, Figure 26). In contrast, the transit duration T of a small obstructing object across the stellar disk scales as $T \propto R_{\star}(P/M_{\star})^{1/3}$ (Winn 2010). While the shortest period ≈ 0.5 -day transient flux dip stars have dip durations consistent with point sources, at longer periods of 1 to 5 days the dip durations become many hours, which is too long to be caused by planetary transits.

Second, approximately 40–50% of the transient flux dip stars discovered in ρ Oph and Upper Sco show two Lomb-Scargle periods, a possible sign of binarity (Stauffer et al. 2017, Table 1). This is higher than the main-sequence companion fraction of $CF_{0.1-0.5 M_{\odot}}^{\text{MS}} = 33 \pm 5\%$, which could be an indication that the transient flux dip phenomenon is linked to stellar binarity (Henry et al. 2006; Duchêne & Kraus 2013; Winters et al. 2019). This fraction might be even more significant given the selection bias against high mass ratio binaries, in which the second star would be too faint to detect a second period.

However, the association between transient flux dips and binarity is not iron-clad. Firstly, multiple photometric periods do not necessarily imply binarity. For instance, circumstellar material could exist around single stars at multiple orbital distances, and not just at the co-rotation radius. This could cause eclipses with periods different from the stellar rotation period. Additionally, low-mass pre-main-sequence stars have been shown to have companion fractions up to twice as high in dispersed clusters such as Upper Sco and Taurus (Kraus et al. 2008, 2011). A high-resolution imaging survey would be interesting, to determine whether the transient flux dip stars truly have distinct population-level binarity properties relative to other young low-mass stars.

5.4. Physical Interpretation

The evidence for binarity in PTFO8-8695 is as follows. First, the star is twice as bright as stars of the same color in its kinematic group (Figure 5). Second, it shows two distinct photometric signals. These points alone suggest binarity (Stauffer et al. 2018). For the case of PTFO8-8695, there is a third line of evidence: the Gaia DR2 entry for PTFO8-8695

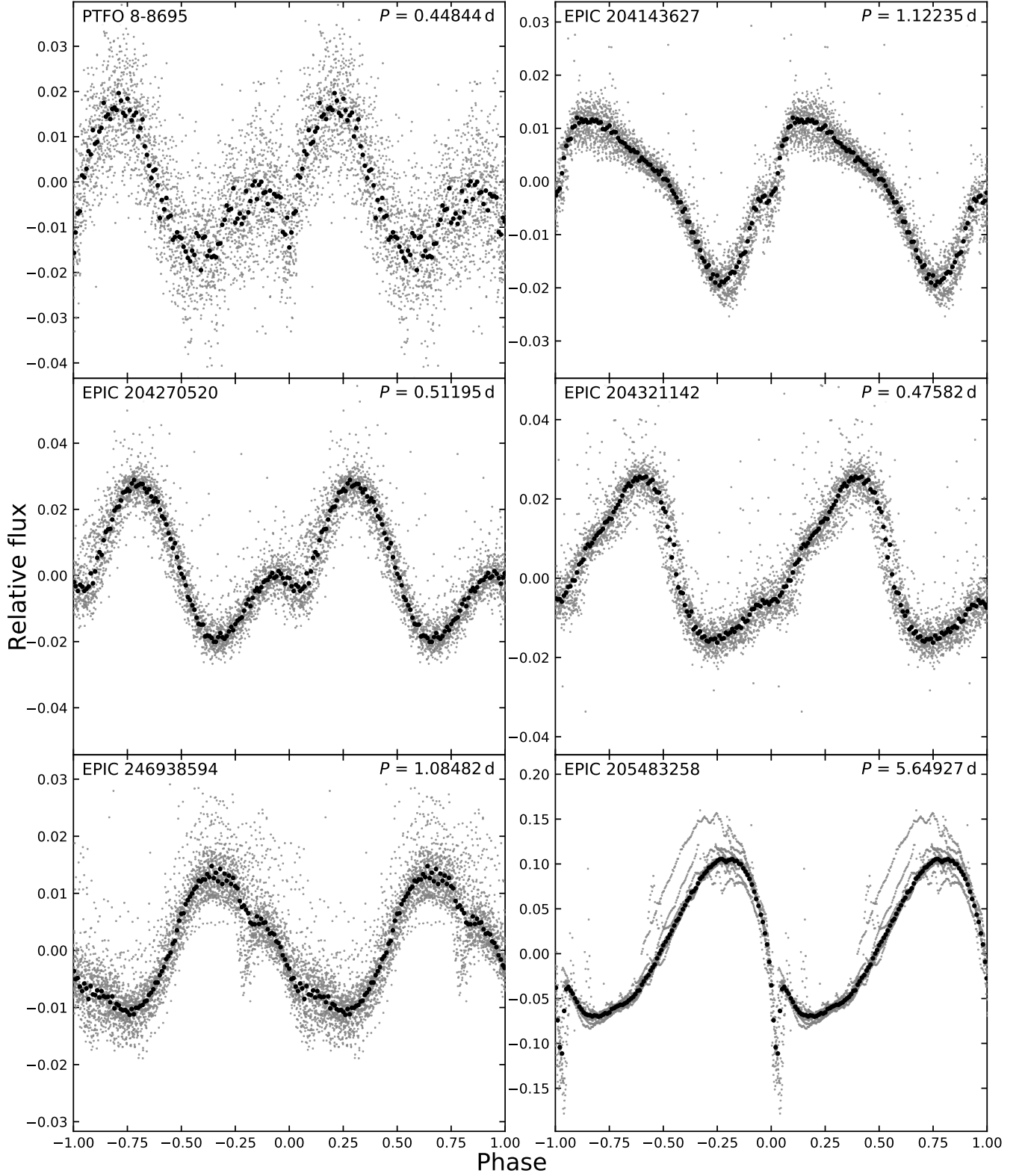


Figure 7. PTFO8-8695 and its brethren. Shown are the light curves of five transient and persistent flux dip stars, selected based on their similarity to the short-period signal of PTFO8-8695. The stars are EPIC 204143627, EPIC 204270520, EPIC 204321142, EPIC 246938594, and EPIC 205483258 (RIK-210). RIK-210 has the longest period of any of these objects. All the analogs displayed are either in Taurus or Upper Sco, and meet the characteristics of Section 5.3.2. These objects were originally reported by [Stauffer et al. \(2017\)](#), [David et al. \(2017\)](#), and [Rebull et al. \(2018\)](#).

reports a poor fit of the single-star model to the astrometric data. While this could be caused by stellar variability, other cluster members that are just as variable do not typically show the same level of excess astrometric motion. Therefore the astrometric excess is a suggestive third line of evidence for binarity in PTFO 8-8695. To us, the evidence leads to the conclusion that PTFO 8-8695 is a nearly equal-mass binary consisting of two rapidly rotating stars.

Based on the lack of an infrared excess seen by Yu et al. (2015), the primordial disks of both stars in PTFO 8-8695 seem to have been depleted of hot dust within the inner ~ 1 AU. This is consistent with the 8.5 ± 1.2 Myr age of the 25 Ori-1 group, and the rapid rate at which stars lose their disks between 1 and 10 Myr (e.g., Hernández et al. 2007). The stars are therefore presumably no longer magnetically locked to their disks. This is also suggested by the \approx half-day periodicities of both rotation signals: young disked M dwarfs typically rotate with periods of two days or more due to magnetic locking (e.g., Rebull et al. 2020). If the two stars are within ≈ 50 AU of each other, as required by the NIRC2 adaptive optics imaging, then it would also be expected that the stars would have truncated the outer edges of their respective disks, in a manner seen at the population level in exoplanetary systems (Kraus et al. 2016; Moe & Kratter 2019).

The key question is what causes the transient dips. This is an unsolved problem not only for PTFO 8-8695 but also for the emerging class of similar young and rapidly rotating M-dwarfs. Many possible explanations were discussed by Rebull et al. (2016), David et al. (2017), Stauffer et al. (2017), and Zhan et al. (2019). Among the *disfavored* explanations are that the dips are caused by (i) eclipsing binaries; (ii) “dipper”-flavor Class-I or Class-II disks; (iii) eclipses of prominences; (iv) high-latitude starspots; or (v) dust clouds of particular compositions (Zhan et al. 2019, Figure 10). We also view the possibility of (vi) tidally disrupted planetary or cometary material to be implausible, given the synchronicity between dip and rotation periods seen across many systems. Finally, (vii) transits of an enshrouded protoplanet can be added to the list of disfavored explanations, based on the chromaticity, asymmetric phase curve, and light-curve changes seen in PTFO 8-8695.

The explanations that we view as not yet ruled out include A) transiting clumps of dust or gas at the Keplerian co-rotation radius; B) occultations of hotspots on the stellar surface by an optically thick disk (Zhan et al. 2019); and C) high-latitude accretion hotspots passing behind the star (Yu et al. 2015). Observations of PTFO 8-8695 over the past decade may offer some hints. PTFO 8-8695’s transition between having no dips, one dip, and multiple dips per cycle seems important (Figure 6). The $H\alpha$ excess observed by Johns-Krull et al. (2016b) also seems like an important piece of evidence.

The high-latitude accretion hotspot scenario seems capable of explaining most of the qualitative characteristics of PTFO 8-8695. Some degree of accretion onto the star seems likely, given the high-velocity (± 200 km s $^{-1}$) components of the observed $H\alpha$ line profile (Johns-Krull et al. 2016b), as

well as the $H\alpha$ equivalent width of 11.4 \AA (van Eyken et al. 2012), which is near the boundary separating “classical” and “weak-lined” T Tauri stars (Briceño et al. 2019). The non-detection of any NIR excess could be problematic, but does not eliminate the possibility that a tenuous amount of dust and gas remains near the star, and is able to accrete onto it. The main problem with this explanation is that it seems to require rare circumstances, making it unlikely to be correct for the entire population of transient flux dips. RIK-210 in particular has dips that seem too deep ($\sim 20\%$) and too asymmetric to be explained by an accretion hot spot (David et al. 2017).

Explanations A and B (circumstellar material at the co-rotation radius, and occultations of spots by a disk) have the appeal that they are flexible enough to explain not only the transient and persistent-dip stars, but also the “scallop shells” (Stauffer et al. 2017). In the spot occultation scenario (Zhan et al. 2019), the “blobs” that provide the necessary brightness contrast are on the surface of the star, rather than at the co-rotation radius. The observing geometry would require an inner ring to be projected into a narrow band in front of the stellar disk, in order to produce variations with sufficiently short timescales. The outer disk would also need to either not be present, or to be misaligned enough and insufficiently flared, that it did not obstruct the line of sight to the star. This geometric requirement seems too contrived to occur in even $\lesssim 1\%$ of young M dwarf systems.

Thus, while several of the proffered explanations deserve further scrutiny, we consider the clumpy torus of optically thick dust or gas near the co-rotation radius to be most plausible. The partially ionized circumstellar hydrogen would readily explain the excess $H\alpha$ emission, and changes in the clumping geometry would lead to changes in the observed eclipse shapes. The long-term stability, punctuated by changes in dip phases, might be understood as an accretion disk subject to strong magnetic fields going through “stalled” states in which material is trapped near co-rotation (D’Angelo & Spruit 2012). Physical models of this scenario may need to consider such states, in addition to dissociation of the dust population (Millan-Gabet et al. 2007; Dullemond & Monnier 2010). Finally, the question of whether the opacity in fact comes from dust or partially-ionized gas (e.g., via gas continuum, atomic lines, or perhaps TiO molecular opacity) remains an additional issue for future exploration.

6. CONCLUSIONS

The combination of TESS and Gaia data has clarified a few things about the PTFO 8-8695 system. Our main results are as follows.

- *The TESS light curve shows two periodic signals.* The “long” signal is a 10% peak-to-peak sinusoid that repeats every 11.98 hr. The “short” signal is a 4% peak-to-peak “dip + asymmetric sinusoid” that repeats every 10.76 hr. The signals beat, and therefore cannot be an artifact linked to data processing. Within the angular resolution of the Gaia source catalog, both signals originate from PTFO 8-8695.

- *The Gaia data imply binarity.* Relative to stars in its kinematic group, PTFO 8-8695 is a photometric binary (Figure 5, top). Relative to stars in its group that are at least as photometrically variable, PTFO 8-8695 also shows signs of astrometric binarity (Figure 5, bottom).
- *The orbital phase of the dip has changed since the discovery by van Eyken et al. (2012).* As shown in Figure 6, the phase seems to have jumped, perhaps twice. This agrees with the recent study by Tanimoto et al. (2020).
- *All properties of PTFO 8-8695 are consistent with the emerging class of transient and persistent flux dip stars.* Analogous light curves are shown in Figure 7. Properties of this variability class are enumerated in Section 5.3.2.

The physical mechanism that explains the transient and persistent flux dips is unresolved. Our preferred explanation is that a clumpy torus of dust or gas is near the Keplerian co-rotation radius, and periodically occults the star. The chromaticity, out-of-eclipse variability, and jumping orbital phase of PTFO 8-8695 all disfavor the explanation of an enshrouded, transiting protoplanet. Though PTFO 8-8695 may not be a planet, understanding it and its analogs is a worthy problem that seems likely to provide insight into how gas and dust disperse from young protostellar disks. Understanding this process would, in turn, teach us about the birth environments of the majority of habitable-zone Earth-sized planets (Dressing & Charbonneau 2013).

When this manuscript was at an advanced stage, we received notice of a paper by Koen (2020) that was in press at the *Monthly Notices* before submission of our manuscript. Our studies independently reached the same conclusions: the TESS light curve shows two periodic signals, and the properties of PTFO 8-8695 are consistent with the emerging class of transient and persistent flux dip stars. Koen (2020) reached these conclusions by modeling the TESS light curve as a truncated sum of Fourier terms, and concluded that the

two signals are most simply interpreted as coming from two stars. Our analysis of the Gaia data provides independent support for the conclusion that PTFO 8-8695 is a binary. We also note the agreement between the TESS dip ephemeris and that from Tanimoto et al. (2020).

The authors thank D. Fabrycky, S. Mahadevan, G. Stefánsson, and A. Vanderburg for helpful calculations, observations, and suggestions. We also thank the Heising-Simons Foundation for their generous support of this work. PTFO 8-8695 was included on the TESS “short-cadence” target list thanks to the Guest Investigator programs of S. Czesla and C. Huang (G011128 and G011132 respectively). Resources supporting this work were provided by the NASA High-End Computing (HEC) Program through the NASA Advanced Supercomputing (NAS) Division at Ames Research Center for the production of the SPOC data products. The Digitized Sky Survey was produced at the Space Telescope Science Institute under U.S. Government grant NAG W-2166. Figure 4 is based on photographic data obtained using the Oschin Schmidt Telescope on Palomar Mountain.

Software: *astrobase* (Bhatti et al. 2018), *astropy* (Astropy Collaboration et al. 2018), *astroquery* (Ginsburg et al. 2018), *cdips-pipeline* (Bhatti et al. 2019), *corner* (Foreman-Mackey 2016), *exoplanet* (Agol et al. 2020), *exoplanet* (Foreman-Mackey et al. 2020), and its dependencies (Agol et al. 2020; Kipping 2013; Luger et al. 2019; Theano Development Team 2016), *IPython* (Pérez & Granger 2007), *lightcurve* (Lightcurve Collaboration et al. 2018), *matplotlib* (Hunter 2007), *MESA* (Paxton et al. 2011, 2013, 2015), *numpy* (Walt et al. 2011), *pandas* (McKinney 2010), *pyGAM* (Servén et al. 2018), *PyMC3* (Salvatier et al. 2016), *scipy* (Jones et al. 2001), *SPOC R4.0* (Jenkins et al. 2016), *tesscut* (Brasseur et al. 2019), *wotan* (Hippke et al. 2019).

Facilities: *Astrometry:* Gaia (Gaia Collaboration et al. 2016, 2018). *Imaging:* Second Generation Digitized Sky Survey, Keck:II (NIRC2; www2.keck.hawaii.edu/inst/nirc2). *Spectroscopy:* Keck:I (HIRES; Vogt et al. 1994). *Photometry:* TESS (Ricker et al. 2015).

Table 1. Model Comparison.

Description	N_s	N_ℓ	N_{data}	N_{param}	χ^2	χ^2_{red}	BIC	ΔBIC
Favored	3	2	2585	21	3102.4	1.210	3267.4	0.0
Disfavored	2	3	2585	21	3179.0	1.240	3344.0	76.6
—	2	2	2585	19	3237.4	1.262	3386.7	119.3
—	3	3	2585	23	3217.1	1.256	3397.9	130.4
—	2	1	2585	17	3312.6	1.290	3446.1	178.7

Table 1 continued

Table 1 (*continued*)

Description	N_s	N_ℓ	N_{data}	N_{param}	χ^2	χ^2_{red}	BIC	ΔBIC
—	3	1	2585	19	3397.5	1.324	3546.8	279.4
—	1	2	2585	17	4101.2	1.597	4234.8	967.3
—	1	3	2585	19	4160.8	1.622	4310.1	1042.7
—	1	1	2585	15	4318.4	1.680	4436.2	1168.8

NOTE— N_s and N_ℓ are the number of harmonics at the short and long periods, respectively. N_{data} is the number of fitted flux measurements. N_{param} is the number of free parameters in the model. The Bayesian information criterion (BIC) and the difference from the maximum ΔBIC are also listed.

Table 2. Best-fit model priors and posteriors.

Param.	Unit	Prior	Mean	Std. Dev.	3 rd Pct.	97 th Pct.
<i>Sampled</i>						
P_s	d	$\mathcal{N}(0.4485; 0.0010)$	0.4484613	0.0000460	0.4483731	0.4485416
$t_s^{(1)}$	d	$\mathcal{N}(0.438096; 0.0020)$	0.4388368	0.0011286	0.4367929	0.4410297
R_p/R_\star	—	$\mathcal{N}(0.1100; 0.0110)$	0.11171	0.00679	0.09950	0.12437
b	—	$\mathcal{U}(0; 1 + R_p/R_\star)$	0.8205	0.0523	0.7188	0.9071
u_1	—	(2)	0.693	0.501	0.	1.638
u_2	—	(2)	-0.01	0.429	-0.804	0.806
Mean	—	$\mathcal{U}(-0.01; 0.01)$	-0.001019	0.000185	-0.001365	-0.000669
R_\star	R_\odot	$\mathcal{T}(1.23; 0.40)$	1.20	0.40	0.44	1.90
M_\star	M_\odot	$\mathcal{T}(0.39; 0.25)$	0.42	0.22	0.	0.78
$A_{s,0}$	—	$\mathcal{U}(-0.02; 0.02)$	0.009083	0.000371	0.008396	0.009763
$B_{s,0}$	—	$\mathcal{U}(-0.02; 0.02)$	0.009696	0.000391	0.008914	0.010352
$A_{s,1}$	—	$\mathcal{U}(-0.02; 0.02)$	0.001646	0.000351	0.000990	0.002297
$B_{s,1}$	—	$\mathcal{U}(-0.02; 0.02)$	-0.005456	0.000307	-0.005998	-0.004861
$A_{s,2}$	—	$\mathcal{U}(-0.02; 0.02)$	0.000177	0.000252	-0.000295	0.000655
$B_{s,2}$	—	$\mathcal{U}(-0.02; 0.02)$	-0.000581	0.000271	-0.001110	-0.0001
ϕ_ℓ	rad	$\mathcal{U}(1.3721; 2.1575)$	1.80542	0.20468	1.47712	2.09634
ω_ℓ	rad d ⁻¹	$\mathcal{N}(12.6054; 0.1261)$	12.588753	0.000972	12.586968	12.590517
$A_{\ell,0}$	—	$\mathcal{U}(-0.06; 0.06)$	0.03929	0.004331	0.031501	0.045035
$B_{\ell,0}$	—	$\mathcal{U}(-0.06; 0.06)$	0.019891	0.008161	0.0071	0.032232
$A_{\ell,1}$	—	$\mathcal{U}(-0.02; 0.02)$	0.002189	0.000516	0.001203	0.003021
$B_{\ell,1}$	—	$\mathcal{U}(-0.02; 0.02)$	-0.002311	0.000496	-0.003063	-0.001364
<i>Derived</i>						
ω_s	rad d ⁻¹	—	14.01054	0.00144	14.00803	14.01330
R_p	R_{Jup}	—	1.30	0.44	0.53	2.16
a/R_\star	—	—	1.81	3.17	0.35	3.29

Table 2 continued

Table 2 (continued)

Param.	Unit	Prior	Mean	Std. Dev.	3 rd Pct.	97 th Pct.
--------	------	-------	------	-----------	----------------------	-----------------------

\mathcal{U} denotes a uniform distribution, \mathcal{N} a normal distribution, and \mathcal{T} a truncated normal bounded between zero and an upper limit much larger than the mean. Note that R_p/R_* has been corrected for the dilution by Star A and other neighboring stars, according to the PDCSAP lightcurve’s CROWDSAP value (0.73) in the optimal aperture. (1) To convert mean TESS mid-transit time to BJD_{TDB} , add 2458468.2. (2) Quadratic limb-darkening prior from Kipping (2013), implemented by Foreman-Mackey et al. (2020).

REFERENCES

- Agol, E., Luger, R., & Foreman-Mackey, D. 2020, *AJ*, **159**, 123
- Ansdell, M., Gaidos, E., Rappaport, S. A., et al. 2016, *ApJ*, **816**, 69
- Astropy Collaboration, Price-Whelan, A. M., Sipőcz, B. M., et al. 2018, *AJ*, **156**, 123
- Barnes, J. W., van Eyken, J. C., Jackson, B. K., Ciardi, D. R., & Fortney, J. J. 2013, *ApJ*, **774**, 53
- Belokurov, V., Penoyre, Z., Oh, S., et al. 2020, *MNRAS*, **496**, 1922
- Bhatti, W., Bouma, L., & Yee, S. 2019, *cdips-pipeline* v0.1.0, <https://doi.org/10.5281/zenodo.3370324>
- Bhatti, W., Bouma, L. G., & Wallace, J. 2018, *astrobases*, <https://doi.org/10.5281/zenodo.1469822>
- Biddle, L. I., Johns-Krull, C. M., Llama, J., Prato, L., & Skiff, B. A. 2018, *ApJL*, **853**, L34
- Blanton, M. R., Bershad, M. A., Abolfathi, B., et al. 2017, *AJ*, **154**, 28
- Bodman, E. H. L., Quillen, A. C., Ansdell, M., et al. 2017, *MNRAS*, **470**, 202
- Bouma, L. G., Hartman, J. D., Bhatti, W., Winn, J. N., & Bakos, G. Á. 2019, *ApJS*, **245**, 13
- Brasseur, C. E., Phillip, C., Fleming, S. W., Mullally, S. E., & White, R. L. 2019, *Astrophysics Source Code Library*, [ascl:1905.007](https://ui.adsabs.org/abs/2019ASCI..1905007B)
- Briceño, C., Calvet, N., Hernández, J., et al. 2005, *AJ*, **129**, 907
- Briceño, C., Hartmann, L., Hernández, J., et al. 2007, *ApJ*, **661**, 1119
- Briceño, C., Preibisch, T., Sherry, W. H., et al. 2007, in *Protostars and Planets V*, ed. B. Reipurth, D. Jewitt, & K. Keil, 345
- Briceño, C., Calvet, N., Hernández, J., et al. 2019, *AJ*, **157**, 85
- Bryson, S. T., Jenkins, J. M., Klaus, T. C., et al. 2020, *Kepler Data Processing Handbook: Target and Aperture Definitions: Selecting Pixels for Kepler Downlink*, *Kepler Data Processing Handbook (KSCI-19081-003)*
- Burnham, K. P., & Anderson, D. R. 2016, *Sociological Methods & Research*
- Ciardi, D. R., Eyken, J. C. v., Barnes, J. W., et al. 2015, *ApJ*, **809**, 42
- Cody, A. M., & Hillenbrand, L. A. 2018, *AJ*, **156**, 71
- Cottle, J., Covey, K. R., Suárez, G., et al. 2018, *ApJS*, **236**, 27
- Cropper, M., Katz, D., Sartoretti, P., et al. 2018, *A&A*, **616**, A5
- D’Angelo, C. R., & Spruit, H. C. 2012, *MNRAS*, **420**, 416
- David, T. J., Petigura, E. A., Hillenbrand, L. A., et al. 2017, *ApJ*, **835**, 168
- Donati, J. F., Moutou, C., Malo, L., et al. 2016, *Nature*, **534**, 662
- Donati, J.-F., Yu, L., Moutou, C., et al. 2017, *Monthly Notices of the Royal Astronomical Society*, **465**, 3343
- Dressing, C. D., & Charbonneau, D. 2013, *ApJ*, **767**, 95
- Duchêne, G., & Kraus, A. 2013, *ARA&A*, **51**, 269
- Dullemond, C. P., & Monnier, J. D. 2010, *ARA&A*, **48**, 205
- Evans, D. W., Riello, M., De Angeli, F., et al. 2018, *A&A*, **616**, A4
- Fang, M., van Boekel, R., Wang, W., et al. 2009, *a*, **504**, 461
- Flagg, L., Johns-Krull, C. M., Nofi, L., et al. 2019, *ApJ*, **878**, L37
- Foreman-Mackey, D. 2016, *Journal of Open Source Software*, **1**, 24
- Foreman-Mackey, D., Czekala, I., Luger, R., et al. 2020, *exoplanet-dev/exoplanet* v0.2.6
- Gaia Collaboration, Prusti, T., de Bruijne, J. H. J., et al. 2016, *A&A*, **595**, A1
- Gaia Collaboration, Brown, A. G. A., Vallenari, A., et al. 2018, *A&A*, **616**, A1
- Gelman, A., & Rubin, D. B. 1992, *Statistical Science*, **7**, 457
- Ginsburg, A., Sipocz, B., Madhura Parikh, et al. 2018, *Astropy/Astroquery: V0.3.7 Release*, <https://zenodo.org/record/1160627>
- Gunn, J. E., Siegmund, W. A., Mannery, E. J., et al. 2006, *AJ*, **131**, 2332
- Henry, T. J., Jao, W.-C., Subasavage, J. P., et al. 2006, *AJ*, **132**, 2360
- Hernández, J., Calvet, N., Briceño, C., et al. 2007, *ApJ*, **671**, 1784
- Hippke, M., David, T. J., Mulders, G. D., & Heller, R. 2019, *AJ*, **158**, 143
- Hoffman, M. D., & Gelman, A. 2014, *Journal of Machine Learning Research*, **15**, 1593
- Howarth, I. D. 2016, *MNRAS*, **457**, 3769
- Howell, S. B., Sobeck, C., Haas, M., et al. 2014, *PASP*, **126**, 398
- Hunter, J. D. 2007, *Computing in Science & Engineering*, **9**, 90
- Jeffries, R. D., Maxted, P. F. L., Oliveira, J. M., & Naylor, T. 2006, *MNRAS*, **371**, L6

- Jenkins, J. M., Twicken, J. D., McCauliff, S., et al. 2016, *Software and Cyberinfrastructure for Astronomy IV*, 9913, 99133E
- Johns-Krull, C. M., McLane, J. N., Prato, L., et al. 2016a, *ApJ*, 826, 206
- Johns-Krull, C. M., Prato, L., McLane, J. N., et al. 2016b, *ApJ*, 830, 15
- Jones, E., Oliphant, T., Peterson, P., et al. 2001, Open source scientific tools for Python
- Kamiaka, S., Masuda, K., Xue, Y., et al. 2015, *Publications of the Astronomical Society of Japan*, 67, 94
- Kipping, D. M. 2013, *MNRAS*, 435, 2152
- Koen, C. 2015, *MNRAS*, 450, 3991
- Koen, C. 2020, *MNRAS*
- Kounkel, M., Covey, K., Suárez, G., et al. 2018, *AJ*, 156, 84
- Kraus, A. L., Ireland, M. J., Huber, D., Mann, A. W., & Dupuy, T. J. 2016, *AJ*, 152, 8
- Kraus, A. L., Ireland, M. J., Martinache, F., & Hillenbrand, L. A. 2011, *ApJ*, 731, 8
- Kraus, A. L., Ireland, M. J., Martinache, F., & Lloyd, J. P. 2008, *ApJ*, 679, 762
- Lee, C.-H., & Chiang, P.-S. 2018, *ApJL*, 852, L24
- Lightkurve Collaboration, Cardoso, J. V. d. M., Hedges, C., et al. 2018, Lightkurve: Kepler and TESS time series analysis in Python, Astrophysics Source Code Library, [ascl:1812.013](https://arxiv.org/abs/1812.013)
- Lindgren, L., Hernández, J., Bombrun, A., et al. 2018, *a*, 616, A2
- Lomb, N. R. 1976, *Astrophysics and Space Science*, 39, 447
- Luger, R., Agol, E., Foreman-Mackey, D., et al. 2019, *AJ*, 157, 64
- Luger, R., Agol, E., Kruse, E., et al. 2016, *AJ*, 152, 100
- Luger, R., Kruse, E., Foreman-Mackey, D., Agol, E., & Saunders, N. 2018, *AJ*, 156, 99
- Majewski, S. R., Schiavon, R. P., Frinchaboy, P. M., et al. 2017, *AJ*, 154, 94
- Maucó, K., Briceño, C., Calvet, N., et al. 2018, *The Astrophysical Journal*, 859, 1
- McKinney, W. 2010, in *Proceedings of the 9th Python in Science Conference*, ed. S. van der Walt & J. Millman, 51
- Millan-Gabet, R., Malbet, F., Akeson, R., et al. 2007, in *Protostars and Planets V*, ed. B. Reipurth, D. Jewitt, & K. Keil, 539
- Moe, M., & Kratter, K. M. 2019, [arXiv:1912.01699 \[astro-ph\]](https://arxiv.org/abs/1912.01699), [arXiv: 1912.01699](https://arxiv.org/abs/1912.01699)
- Onitsuka, M., Fukui, A., Narita, N., et al. 2017, *PASJ*, 69
- Parks, J. R., Plavchan, P., White, R. J., & Gee, A. H. 2014, *ApJS*, 211, 3
- Paxton, B., Bildsten, L., Dotter, A., et al. 2011, *ApJS*, 192, 3
- Paxton, B., Cantiello, M., Arras, P., et al. 2013, *ApJS*, 208, 4
- Paxton, B., Marchant, P., Schwab, J., et al. 2015, *ApJS*, 220, 15
- Pérez, F., & Granger, B. E. 2007, *Computing in Science and Engineering*, 9, 21
- Raetz, S., Schmidt, T. O. B., Czesla, S., et al. 2016, *MNRAS*, 460, 2834
- Rebull, L. M., Stauffer, J. R., Cody, A. M., et al. 2020, *AJ*, 159, 273
- . 2018, *AJ*, 155, 196
- Rebull, L. M., Stauffer, J. R., Bouvier, J., et al. 2016, *AJ*, 152, 114
- Ricker, G. R., Winn, J. N., Vanderspek, R., et al. 2015, *Journal of Astronomical Telescopes, Instruments, and Systems*, 1, 014003
- Rizzuto, A. C., Vanderburg, A., Mann, A. W., et al. 2018, *AJ*, 156, 195
- Salvatier, J., Wiecki, T. V., & Fonnesbeck, C. 2016, PyMC3: Python probabilistic programming framework
- Scargle, J. D. 1982, *ApJ*, 263, 835
- Schmidt, T. O. B., Neuhauser, R., Briceño, C., et al. 2016, *A&A*, 593, A75
- Servén, D., Brummitt, C., & Abedi, H. 2018, *dswah/pyGAM: v0.8.0*
- Shporer, A. 2017, *PASP*, 129, 072001
- Smith, J. C., Stumpe, M. C., Cleve, J. E. V., et al. 2012, *PASP*, 124, 1000
- Stassun, K. G., Oelkers, R. J., Pepper, J., et al. 2018, *AJ*, 156, 102
- Stassun, K. G., Oelkers, R. J., Paegert, M., et al. 2019, *AJ*, 158, 138
- Stauffer, J., Rebull, L. M., Cody, A. M., et al. 2018, *AJ*, 156, 275
- Stauffer, J., Cody, A. M., McGinnis, P., et al. 2015, *AJ*, 149, 130
- Stauffer, J., Cameron, A. C., Jardine, M., et al. 2017, *AJ*, 153, 152
- Stumpe, M. C., Smith, J. C., Catanzarite, J. H., et al. 2014, *PASP*, 126, 100
- Tanimoto, Y., Yamashita, T., Ui, T., et al. 2020, *PASJ*, 72, 23
- Tenenbaum, P., & Jenkins, J. 2018, TESS Science Data Products Description Document, EXP-TESS-ARC-ICD-0014 Rev D, <https://archive.stsci.edu/missions/tess/doc/EXP-TESS-ARC-ICD-TM-0014.pdf>
- Theano Development Team. 2016, *arXiv e-prints*, [abs/1605.02688](https://arxiv.org/abs/1605.02688)
- van Eyken, J. C., Ciardi, D. R., von Braun, K., et al. 2012, *ApJ*, 755, 42
- VanderPlas, J. T., & Ivezić, Z. 2015, *ApJ*, 812, 18
- Vogt, S. S., Allen, S. L., Bigelow, B. C., et al. 1994, *SPIE Conference Series*, ed. D. L. Crawford & E. R. Craine, Vol. 2198
- Walt, S. v. d., Colbert, S. C., & Varoquaux, G. 2011, *Computing in Science & Engineering*, 13, 22
- Winn, J. N. 2010, in *Exoplanets*, ed. S. Seager (Tucson, AZ: University of Arizona Press), 55
- Winters, J. G., Henry, T. J., Jao, W.-C., et al. 2019, *AJ*, 157, 216
- Wright, E. L., Eisenhardt, P. R. M., Mainzer, A. K., et al. 2010, *AJ*, 140, 1868
- Yu, L., Winn, J. N., Gillon, M., et al. 2015, *ApJ*, 812, 48
- Yu, L., Donati, J.-F., Hébrard, E. M., et al. 2017, *Monthly Notices of the Royal Astronomical Society*, 467, 1342
- Zasowski, G., Cohen, R. E., Chojnowski, S. D., et al. 2017, *AJ*, 154, 198
- Zhan, Z., Günther, M. N., Rappaport, S., et al. 2019, *ApJ*, 876, 127
- Ziegler, C., Law, N. M., Baranec, C., et al. 2018, *AJ*, 156, 259